Article

Digital Quantitative Study on Fracture Gas Storage Space for a Three-Layer Composite Residual Mining Area

Guorui Feng [1,2,3], Weichao Fan [1,2,3], Zhen Li [2,3,4,*], Zhiwei Wang [1,2,3], Yidie Zhang [1,2,3], Yanqun Yang [5], Xiaohong Yang [5], Xiangming Zhang [4] and Gan Feng [6]

[1] College of Mining Engineering, Taiyuan University of Technology, Taiyuan 030024, China
[2] Key Laboratory of Shanxi Province for Mine Rock Strata Control and Disaster Prevention, Taiyuan 030024, China
[3] Shanxi Province Coal-Based Resources Green and High-Efficiency Development Engineering Center, Taiyuan 030024, China
[4] College of Safety and Emergency Management Engineering, Taiyuan University of Technology, Taiyuan 030024, China
[5] Shanxi Coking Coal Group Co., Ltd., Taiyuan 030024, China
[6] State Key Laboratory of Hydraulics and Mountain River Engineering, College of Water Resource & Hydropower, Sichuan University, Chengdu 610065, China
* Correspondence: lizhen@tyut.edu.cn

Abstract: Quantifying the fracture gas storage space is the key to improving the coalbed methane (CBM) extraction efficiency in residual mining areas (RMAs). In this paper, a new digital quantitative description method of fractures is proposed when using a digital image correlation (DIC) system to monitor strata displacement, which improves the accuracy of fracture statistical data. The results show that with the evolution of RMA from single to three layers, the rock strata area with displacement greater than 3.5 mm increases radially and the maximum fracture rate of the uppermost RMA increases by 64.26%. The fracture rate increases exponentially from top to bottom in a long-distance composite RMA and distributes parabolically in the horizontal partition. The area with the highest average fracture rate (12.65%) in the close-distance composite RMA is defined as the concentrated growth area. The longitudinal fracture rate of a cross-layer fracture area in the three-layer RMA exceeds 60%. The cross-layer fracture area connecting the composite RMA at the open-cut side is a favorable extraction location for surface drilling. The research results will provide theoretical support for the safe and sustainable exploitation of CBM and residual coal in composite RMA.

Keywords: coalbed methane; gas storage space; fracture development; digitization; sustainable

1. Introduction

Coal has been in the dominant position of China's energy structure for a long time, but the contradiction between limited resources and unlimited demand is becoming increasingly prominent [1,2]. Due to the limitations of history, technology, and economic conditions, the research of USGS and EIA shows that the mining output only accounts for 50~60% of the proved reserves [3]. According to statistics, the total amount of coal in China's residual mining areas (RMAs) has reached approximately 40 billion tons. Much residual coal is bound to desorb abundant coalbed methane (CBM) in the RMAs [3–6]. The types of residual mining areas are mostly multi-layer composites, the Yangquan Coal Mine No. 3 in China being a typical case. Reasonable control and development of CBM can also effectively prevent and reduce mine geological disasters, especially gas outburst accidents [7–9]. Meanwhile, CBM is a clean and high-quality geological resource; thus, green and sustainable exploitation of residual coal and CBM is an important measure to address the problem of energy shortage [10–14]. Clarifying the enrichment location for CBM in the composite RMA is the basis for safe and efficient extraction. However,

the desorbed CBM in the RMA is stored in the place where the overburden fractures are developed. Therefore, it is of great significance to quantitatively analyze and study the fracture gas storage space in composite RMA.

In the 1980s and 1990s, some scholars put forward classical theories about the displacement evolution and fracture development characteristics of overlying strata caused by single-layer longwall mining [15–19]. Later, based on the "O-shape" theory of mining-induced fracture, Li and Lin put forward the model of mining-induced fracture elliptic paraboloid zone [20], and both Qin and Xie studied the influence of mining thickness on fracture development [21,22]. Xu et al. proposed a new "three zones" theory of gas pressure relief and drainage [23]. Karacan and Goodman found that the probability of fracturing and bedding plane separations in the overburden increase between strong and weak rock interfaces [24]. Liu and Xu used fractal geometry theory to study the overburden fracture network and fracture opening [25,26]. Majdi A. and Poulsen both studied the development mechanism of fracture zone height above the goaf roof [27,28]. Li et al. carried out a regional division of CBM storage space in a single-layer abandoned mine gob [29], which contributed to the exploitation of CBM in an abandoned gob.

Relevant research on single coal seam mining has been relatively complete. On this basis, scholars gradually began to study the overburden displacement and fracture development characteristics in the mining of two or more coal seams that are closer to the actual conditions. Xu and Liu pointed out that the close-distance coal seams will have a significant impact on each other and surrounding strata during the mining process [30,31]. Li and Ma studied the pressure relief mining of two layers of coal in a short distance. They found that the fracture is a three-dimensional staggered gas migration channel, and the overburden strata show the characteristics of coordinated migration of multiple strata as a whole [32,33]. Karacan and Hu presented a dynamic 3D reservoir model through their research on multi-seam longwall mining and found that the development degree of overburden fractures would be affected by the composite thickness of coal seams, interlayer spacing, and mining sequence [34,35]. Meanwhile, Si et al. found that the floor coal and roof goaf fractures may both play major roles in the total gas emitted during mining [36]. Qin et al. found that the ground drilling arranged in the O-shaped fracture zone has a greater control range for CBM in the goaf [37,38]. For the repeated mining of shallow coal seams, Zhuo and Huang found that the overburden fractures are mainly the upward vertical fractures developed at the edge of the goaf and the horizontal fractures in the collapse area [39,40]. Tian et al. found that the loss of leakage drilling can reflect the development degree of multi-seam mining roof cracks [41]. Liu et al. studied the development height and evolution process of the overburden fracture after the mining of the Taiyuan Group coal seam [42]. Wu et al. obtained the subsidence curve of the overburden strata and concluded that repeated mining resulted in a significant increase in the overburden fracture rate [43].

With the progress of technical means, scholars began to use optical equipment and computer systems to conduct digital image analysis and research on various things such as strata displacement and fracture evolution [44–47]. Palamara et al. found that the use of airborne laser scanning (ALS) can improve the spatial coverage of coal mine subsidence information [48]. Feng et al. studied the fracture propagation characteristics of different hard surrounding rocks after excavation and unloading through a two-dimensional FEM/DEM combined method and scanning electron microscope observation [49–51]. Through similar simulation experiments, Smith et al. modeled the ground subsidence caused by multi-seam mining and analyzed it using a digital camera, optical non-contact displacement transducer, and 3D terrestrial laser scanner [52]. Hu et al. studied and obtained the displacement distribution characteristics of overburden rocks using digital image correlation (DIC) image speckle technology [53]. Feng and Zhang used the image binarization method to quantitatively extract the geometric parameters of fractures in the goaf. They found that both longitudinal and horizontal fracture distributions showed normal distribution [54,55]. Wang et al. used the DIC speckle technology to measure the whole displacement field of the overlying strata under different progress rates [56]. Chew et al. proposed an improved

particle swarm optimization algorithm with sub-pixel accuracy for the surface speckle measurement [57]. Xiao et al. investigated the deformation and failure process of deep rock roadways by using the DIC [58]. Yuan et al. studied the geological disasters induced by the mining overburden separation strata by the DIC speckle method [59]. Zhang et al. combined DIC and particle image velocimetry techniques to jointly analyze the deformation mechanism of the open-pit slope mining model [60].

From the above research, it can be seen that optical devices such as DIC are mainly used to measure strain information of objects, and image binarization can extract effective information such as fractures. These two methods have good effects when used independently. However, when the DIC digital speckle technology is used to monitor the change of strata displacement in practice, if the binary image processing method is used to count the number and size of fractures, the statistical results will be very inaccurate. The influence of speckles on the rock surface will cause many fractures to disappear during the noise reduction processing of the experimental image; thus, accurate statistics cannot be determined. In addition, the development characteristics of fracture gas storage space in multi-seam mining are relatively complex, and relatively little research has been done. If gas extraction is carried out blindly, it will cause more energy waste, so these problems need to be solved urgently.

This paper solves the main problems mentioned above. While using the DIC full-field strain measurement system to study the displacement change of each rock stratum, a new method for quantitative analysis of fracture distribution characteristics using image digitization is proposed. The evolution law of fracture development in the three-layer composite RMA gas storage space is revealed. The research results will provide a theoretical basis and safety guarantees for the sustainable exploitation of CBM and the optimization of surface drilling well location in the composite RMA.

2. Engineering Situations

The Yangquan Coal Mine is located on the northeast edge of Qinshui Coalfield. Over the past 100 years, due to backward mining methods and low mining rates, multi-layer composite RMAs were widely distributed here. This paper takes the typical composite caving RMA of Yangquan No. 3 Mine as the research object. The prototype of the experiment is a composite RMA formed by the #3, #12, and #15 main mining seams that have been mined in Yangquan No. 3 Coal Mine. The #3 RMA is located at the top layer, and the mining face contains K7205, K7207, and K7209. The coal seam mined in the #12 RMA is the thinnest and located in the middle of the three-layer RMA, which is 94.25 m away from the #3 RMA above. The lower part of the RMA of the #12 coal seam is the K8206 fully mechanized caving face of the #15 coal seam, which has been mined. The working face elevation of the #15 coal seam is 503.6~596.3 m. The ground elevation, strike length, and inclination length are 1025~1168 m, 1579 m, and 252.2 m, respectively. The average advancing speed of the working face during the mining process is 3 m/d. The net coal thickness is 6.8 m and the dip angle of the coal seam is 1 °~7 °, with an average of 5° [37]. After the three coal seams were mined out, a three-layer composite RMA was formed. In order to facilitate the experiment and subsequent analysis, the prototype mining length of the three-layer coal is simplified to 200 m. Due to the small inclination angle of the coal seam, it is simplified to be a horizontal coal seam. In addition, 50 m coal pillars are reserved on both sides of the mining face to eliminate boundary effects. The vertical distance between layers of the #3 and #12 RMAs is relatively far, belonging to a long-distance two-layer RMA. However, the vertical distance between layers of the #12 and #15 RMAs is only 42.14 m, which belongs to the close-distance two-layer RMA. Then, similar simulation experiments are conducted based on this prototype.

3. Similarity Simulation Experiment Scheme and Digital Analysis Method

3.1. Design of a Similar Model

The two-dimensional physical similarity simulation experimental platform of the Taiyuan University of Technology was used to model the displacement change of each rock stratum structure and the development characteristics of gas storage space fractures. The size of the experimental device was 3 m (length) × 0.2 m (width) × 2 m (height). The surroundings and bottom were constrained by channel steel and two airbag loading systems were applied to the top. The loading range was 0~0.5 MPa and the load deviation was less than 2%. The model material is mainly composed of fine aggregate, binder, and retarder. The fine aggregate is fine sand, while the binder is made of calcium carbonate and gypsum, and the retarder is made of borax to slow down the setting speed of gypsum in the process of mixing so that the model is laid more evenly. The layered material between each rock layer is mica powder. According to the actual geological data and similarity theory of Yangquan Coal Mine strata, the main similarity parameters were as follows [61]:

Geometric similarity ratio:

$$C_l = L_o / L_m = 100 : 1 \tag{1}$$

Time similarity ratio:

$$C_t = T_o / T_m = 10 : 1 \tag{2}$$

Bulk density similarity ratio:

$$C_\gamma = \gamma_o / \gamma_m = 1.5 : 1 \tag{3}$$

Stress similarity ratio:

$$C_\sigma = \sigma_o / \sigma_m = C_l \times C_r = 150 : 1 \tag{4}$$

Considering the size of the experimental device, the model simulation length laid in a similar simulation experiment was set to 3 m. In Formula (1), the prototype size length is L_o, and the corresponding model size is L_m; in Formula (2), the working time of central mining is T_o, and the corresponding experimental simulation is T_m; in Formula (3), the prototype bulk density is γ_o, and the corresponding model bulk density is γ_m.

The actual thickness and material ratio of the coal rock model in the similarity simulation experiment are shown in Figure 1.

The strike length of the model laid by similarity simulation was 300 cm. The left and right sides were set to the 50 cm boundary coal pillar, meaning the strike length of model mining was 200 cm. The actual buried depth at the top of the model was 340.34 m. Therefore, from the similarity principle, the compensation load applied by the pressurized airbag was 0.0544 MPa.

3.2. DIC Full-Field Strain Measurement System

DIC, also known as the digital speckle analysis method, is a new type of non-contact test method for image processing technology in optical strain measurement. The advantages include full-field measurement, non-contact, no environmental impact, and simple operation. Therefore, it has been widely used in the measurement of various physical experiments.

The Xintuo Digital Image Correlation (XTDIC) full-field strain measurement system was used in this experiment. It combines DIC technology and binocular stereo-vision technology. By tracking the image of the selected speckle area on the surface of the object, the three-dimensional coordinates, displacement field, and strain field of the surface of the model during the deformation process can be measured and analyzed. The system consists of a computer workstation supporting XTDIC software, two high-definition cameras, two high-power blue lights, and a balance bracket. The surface of the model is whitened before the model is excavated. The irregularly arranged and evenly distributed scattered spots are

used to calibrate the initial position of the model. The specific experimental layout of the XTDIC system is shown in Figure 2.

Order	Lithology	Thickness /cm	Geological columnar	Material ratio	Sand /kg	Calcium carbonate/kg	Gypsum /kg
1	Siltstone	15.35		5:0.7:0.3	122.80	17.19	7.37
2	Fine sandstone	3.33		8:0.6:0.4	28.42	2.13	1.42
3	Siltstone	6.72		5:0.7:0.3	53.76	7.53	3.23
4	Coarse sandstone	4.00		5:0.5:0.5	32.00	3.20	3.20
5	Siltstone	1.50		5:0.7:0.3	12.00	1.68	0.72
6	Fine sandstone	6.79		8:0.6:0.4	57.94	4.35	2.90
7	Siltstone	1.00		5:0.7:0.3	8.00	1.12	0.48
8	Medium sandstone	4.00		3:0.5:0.5	28.80	4.80	4.80
9	3# coal seam	1.81		9:0.7:0.3	15.64	1.22	0.52
10	Siltstone	1.70		5:0.7:0.3	13.60	1.90	0.82
11	Mudstone	4.39		7:0.7:0.3	36.88	3.69	1.58
12	Siltstone	9.38		5:0.7:0.3	75.04	10.51	4.50
13	Medium sandstone	10.94		3:0.5:0.5	78.77	13.13	13.13
14	Siltstone	6.66		5:0.7:0.3	53.28	7.46	3.20
15	Mudstone	14.68		7:0.7:0.3	123.31	12.33	5.28
16	Fine sandstone	2.50		8:0.6:0.4	21.33	1.60	1.07
17	Coarse sandstone	6.50		5:0.5:0.5	52.00	5.20	5.20
18	Siltstone	15.34		5:0.7:0.3	122.72	17.18	7.36
19	Mudstone	3.40		7:0.7:0.3	28.56	2.86	1.22
20	Medium sandstone	2.36		3:0.5:0.5	16.99	2.83	2.83
21	Siltstone	2.00		5:0.7:0.3	16.00	2.24	0.96
22	Mudstone	3.00		7:0.7:0.3	25.20	2.52	1.08
23	Limestone	2.00		8:0.2:0.8	17.07	0.43	1.71
24	Siltstone	4.40		5:0.7:0.3	35.20	4.93	2.11
25	Silty mudstone	5.00		6:0.7:0.3	41.14	4.80	2.06
26	12# coal seam	1.71		9:0.7:0.3	14.77	1.15	0.49
27	Fine sandstone	2.93		8:0.6:0.4	25.00	1.88	1.25
28	Limestone	6.60		8:0.2:0.8	56.32	1.41	5.63
29	Medium sandstone	16.73		3:0.5:0.5	120.46	20.08	20.08
30	Silty mudstone	3.40		6:0.7:0.3	27.98	3.26	1.40
31	Limestone	2.82		3:0.3:0.7	20.30	2.03	4.74
32	Silty mudstone	3.01		6:0.7:0.3	24.77	2.89	1.24
33	Limestone	1.11		3:0.3:0.7	7.99	0.80	1.86
34	Siltstone	3.23		5:0.7:0.3	25.84	3.62	1.55
35	Limestone	2.31		3:0.3:0.7	16.63	1.66	3.88
36	15# coal seam	6.71		9:0.7:0.3	57.97	4.51	1.93
37	Silty mudstone	3.50		3:0.7:0.3	25.20	5.88	2.52
38	Fine sandstone	7.10		8:0.6:0.4	60.59	4.54	3.03

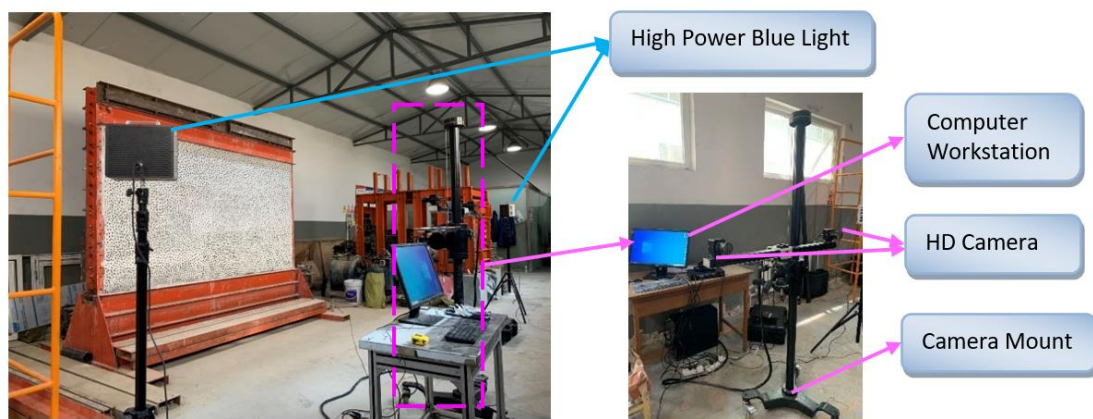**Figure 1.** Thickness and material ratio diagram of similar models.

Figure 2. Experimental layout of the XTDIC system.

3.3. Experimental Process and Digital Processing Method

3.3.1. Similarity Simulation Experimental Process and Monitoring Method

This two-dimensional physical similarity simulation experiment contains two parts, model laying and model excavation.

1. Model laying includes installing the template, batching, stirring, and molding. To prevent too much material from adhering to the inside of the mixer, a manual mixing method is adopted to accurately match the material.
2. The main experimental steps in the excavation process are as follows:

    (1) Before preparing for excavation, open the control software of the XTDIC equipment and record 20 initial displacement photos.
    (2) The simulation time similarity ratio is $C_t = 10$. The actual working face advance is 3 m/d. According to the actual working face '38' operation system, the model simulation time for each shift T_m is 0.8 h. That is, in the simulation, 0.8 h (48 min) is equal to 8 h in the actual working face. Every 48 min will excavate 10 cm in length.
    (3) After each 10 cm excavation, a set of data is recorded with the XTDIC. At the same time, a high-definition camera is used to take photos in a fixed position. The XTDIC photography time is set to record once for 3 s. Therefore, each set of data contains 20 photos in one minute. After recording a series of data, the excavation and data recording are continued until the end of the working face.

3.3.2. Digital Processing Method of Fracture Distribution

The spatial distribution of the overburden fracture rate in composite RMA is an important parameter for measuring the fracture field [43]. To accurately count the distribution characteristics of the fracture field, the analysis processes are as follows. (1) Firstly, the captured high-definition images containing fractures were inserted into the AutoCAD drawing software. (2) The model size in the image is consistent with the actual size in similar simulation experiments (3 m × 2 m) through the proportional scaling function in the AutoCAD software, and then we place the image on the lowest layer and lock it. (3) In this experiment, the red line segments in the AutoCAD software are used to repeatedly manually depict each fracture in the composite residual mining area in the picture, and artificial noise reduction is used to ensure that each fracture and each speckle are distinguished, so as to accurately map the fractures. The red line width specified for use is 2 mm. Coarse fractures with a width greater than 2 mm are processed using the filling function in AutoCAD software (the filling area used the same red color as the line segment) to display its true fracture morphology. (4) The entire composite RMA was partitioned using a 20 × 20 cm grid. The partitioned grid consisted of 9 rows and 12 columns. Here, 1–9 represents the number of vertical partitioned grid rows and A–L represents the number of horizontally partitioned grid columns. (5) The 1–3 rows of the grids were divided into the #3 RMA (represented by the black grid), 4–7 rows of grids were divided into the #12 RMA (represented by the blue grid), and 8–9 rows of grids were divided into the #15 RMA (represented by the orange grid), as shown in Figure 3.

The fracture distribution image was imported into Adobe Photoshop CS6 software while ensuring that the total pixels of the images are equal, the fracture image was evenly divided by its slicing tool using the above-mentioned size grid. After segmentation, the pixels of each picture are effectively the same. The actual side length of each grid was 200 mm, and as the number of pixels along its side length was greater than 100, the statistical accuracy of the fracture could reach within 2 mm.

When dealing with each picture containing fractures, the image histogram function of the software was used to count the pixel value of the fractures based on the specific color, after which the surface fracture rate of each picture was calculated.
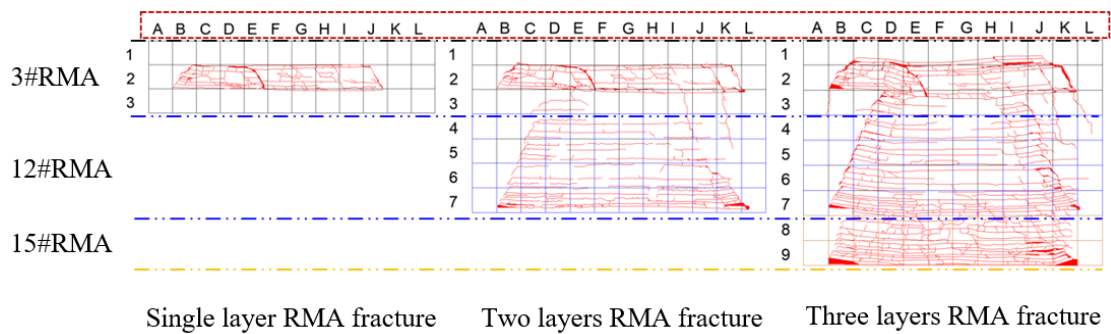
Figure 3. Fracture zoning diagram of the composite RMA.

The formula for calculating the fracture rate x in each grid was Formula (5):

$$x = \frac{\text{Area of fractures in the grid}}{\text{Area of grid}} \times 100\% = \frac{\text{Pixels of fractures in the grid}}{\text{Total grid pixels}} \times 100\% \quad (5)$$

An example taking the distribution of fractures in the two-layer composite RMA is shown in Figure 4. The slice tool is used to evenly divide the image of the whole fracture field into meshes of equal size, and the pixels of length × width in each grid are 102 × 102.
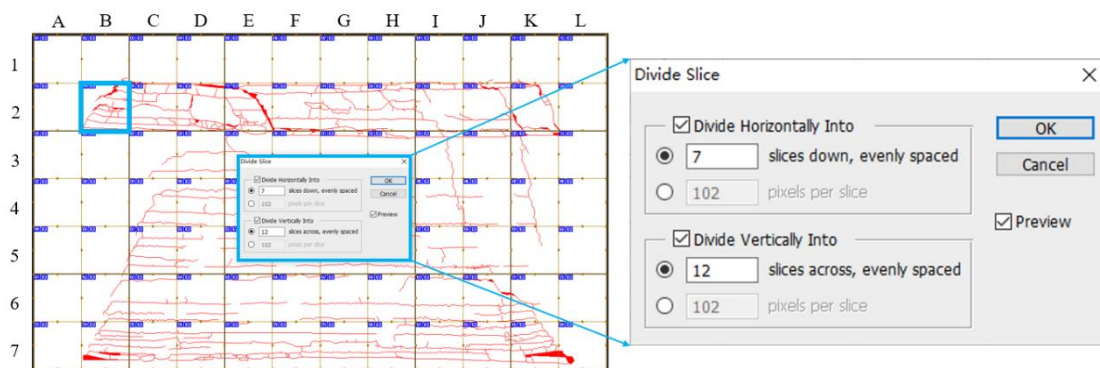
Figure 4. Equal pixel division of fracture field grid.

The calculation process takes the grid numbered B2 as an example. Firstly, the total number of pixels in the B2 grid is calculated as 10,404 using the software histogram, then the red fracture part is selected by color classification for statistics so that there are 929 fracture pixel data. According to the above calculation method, the surface fracture rate of the B2 grid is 8.93%. By analogy, the distribution of fracture rate in the whole composite RMA can be obtained.

4. Results Analysis and Discussion

4.1. Evolution of Rock Strata Displacement in Composite RMA

To quantitatively analyze the displacement of each rock layer, the displacement cloud diagram processed by the XTDIC software (Ver9.5.7_x64) was superimposed on the surface high-definition image of a similar model [53], as shown in Figure 5.

Figure 5 is the displacement distribution cloud diagram of the two-layer composite RMA formed after the mining of the #3 and #12 coal seams. When the #3 coal seam was mined out, violent pressure first appeared on the roof, which caused the appearance of a trapezoidal fracture area on the left side of the overlying strata. This meant that part of the cloud diagram was missing (red box line area). Greater vertical displacement occurred in the overlying strata of the #3 coal seam after the caving of the #12 coal seam. At present, the maximum displacement of the overlying strata of the #3 coal seam has exceeded 30 mm.

The area of overlying strata, which has a displacement greater than 3.5 mm in the #3 RMA, shows an isosceles trapezoid.
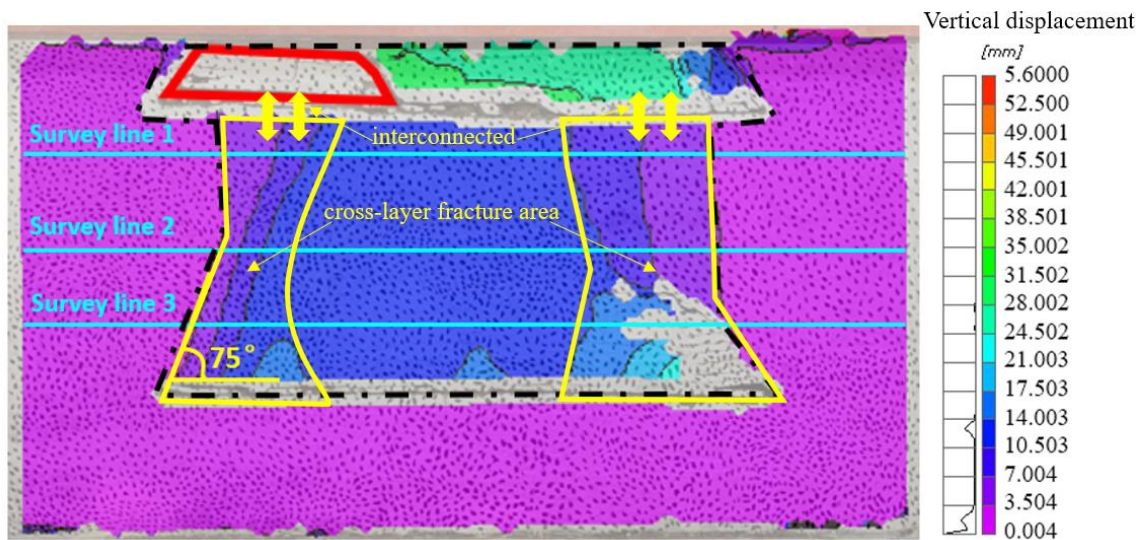
Figure 5. Displacement evolution cloud diagram of the two-layer composite RMA.

The angle between the two side boundaries and the horizontal line is 75°~90° in the area where the displacement of the overlying strata of #12 RMA exceeds 3.5 mm. The change in color scale indicates that the vertical displacement of the rock strata in the central compaction area of the composite RMA is significantly greater than that in the fracture area on either side (Figure 5). The part of the two-layer composite RMA rock stratum with displacement greater than 3.5 mm appears in a two-stacked-trapezoid shape that is wide at the top and bottom and narrow in the middle area (black frame line area).

Figure 6 is the displacement distribution cloud diagram of the three-layer composite RMA. The angle between the two side boundaries of the area with displacement >3.5 mm and the horizontal are obtuse. The area extends upward and shows an inverted ladder shape that is wide at the top and narrow at the bottom (black frame line area). The maximum displacement of the overlying strata in the #3 and #12 RMAs is beyond 56 mm. Obviously, the overlying strata in the #3 RMA are affected by both the #12 and #15 RMAs. Due to #12 and #15 mining activity, violent displacement occurs in the #3 RMA, which results in the absence of the cloud diagram getting larger (red box line area).

The cross-layer fracture (yellow frame line) area was responsible for the largest color changes in the whole composite RMA. The color gradient in the cloud diagram represents the relative displacement of the same horizontal rock layer in the vertical direction. The greater the relative displacement change, the more intense the color gradient change, and at the same time, the more fully developed the fractures are. Obviously, the cross-layer fractures between #3, #12, and #15 are interconnected in the entire three-layer composite RMA, and there is an overlap between the cross-layer fracture regions of each RMA. The larger the overlap, the better the connectivity (as shown by the yellow two-way arrow, more arrows mean better connectivity). These are the main channels for gas migration.

The three survey lines showing statistical rock layer displacement are shown in Figure 7. The survey line in the case of a two-layer RMA is represented by dotted lines, while the survey line in the case of a three-layer RMA is represented by solid lines. Meanwhile, the colors used for the survey lines at the same location are uniform. Obviously, the displacement and change trend of the rock strata in the case of the three-layer composite RMA are larger than that of the two-layer composite RMA at the same survey line. The maximum difference of displacement exceeds 45 mm in the two cases. The absolute value of the displacement curve slope is rather violent in the region of $A_{3\text{-layer}}$ and $B_{3\text{-layer}}$ in the three-layer composite RMA; meanwhile, the intensity and range of its growth and

reduction are greater than those in the $A_{2\text{-layer}}$ and $B_{2\text{-layer}}$ areas in the two-layer RMA. The area with a large absolute value of the curve slope corresponding to the yellow frame line area in Figure 6 implies that this area is the most developed fracture area.
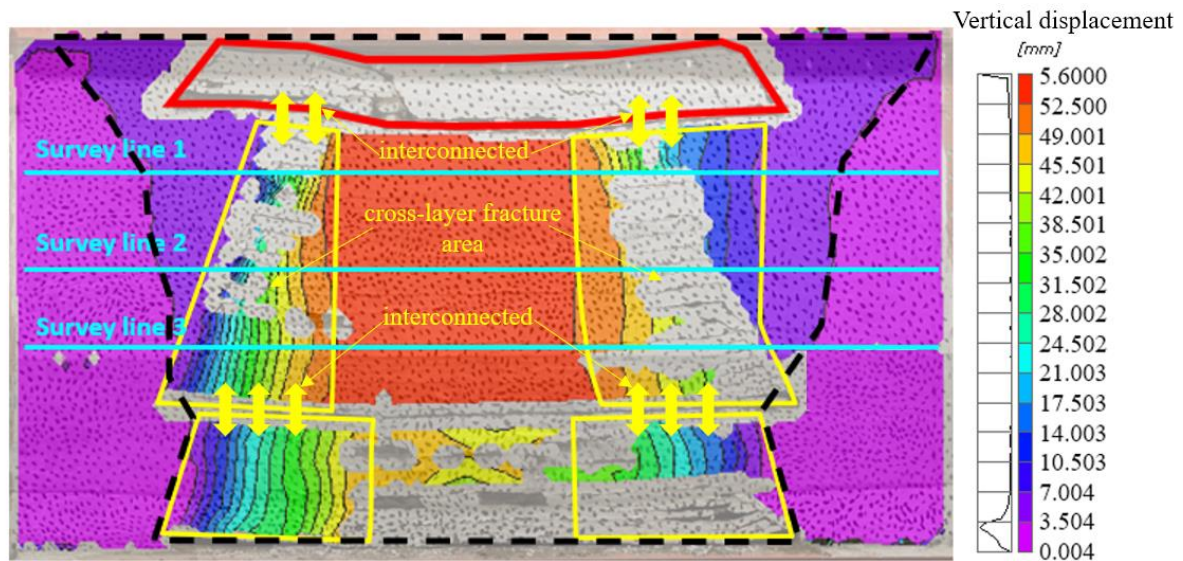

Figure 6. Displacement evolution cloud diagram of the three-layer composite RMA.
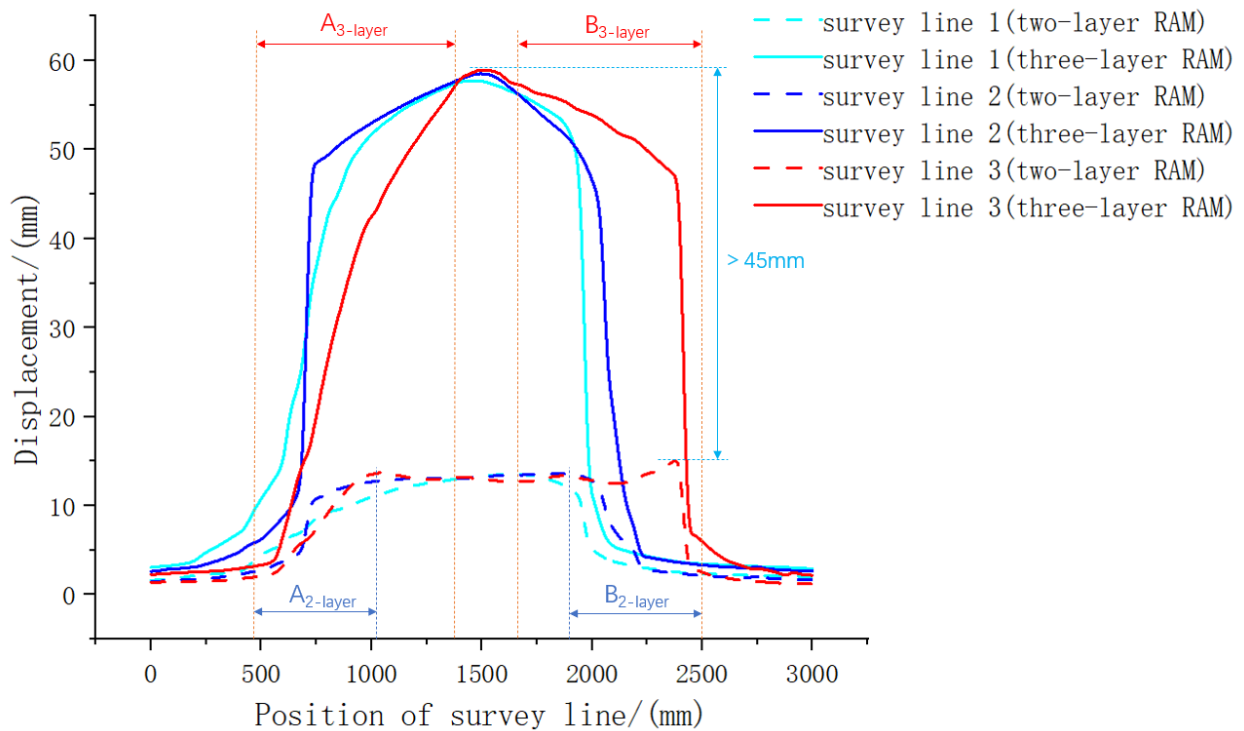

Figure 7. Trend of rock displacement under two conditions.

*4.2. Digital Analysis of Fracture Development in Composite RMA*

4.2.1. Quantitative Analysis of Fracture Field Image

Based on the physical similarity simulation experiment, the fracture data of the composite RMAs were counted and the fracture rate in each grid was calculated. After digital quantitative analysis one by one, the fracture rate evolution development from a single RMA to a double-layer composite RMA and then to a three-layer composite RMA was

obtained. The fracture evolution of the uppermost #3 RMA in the overall composite RMA is shown in Figure 8.
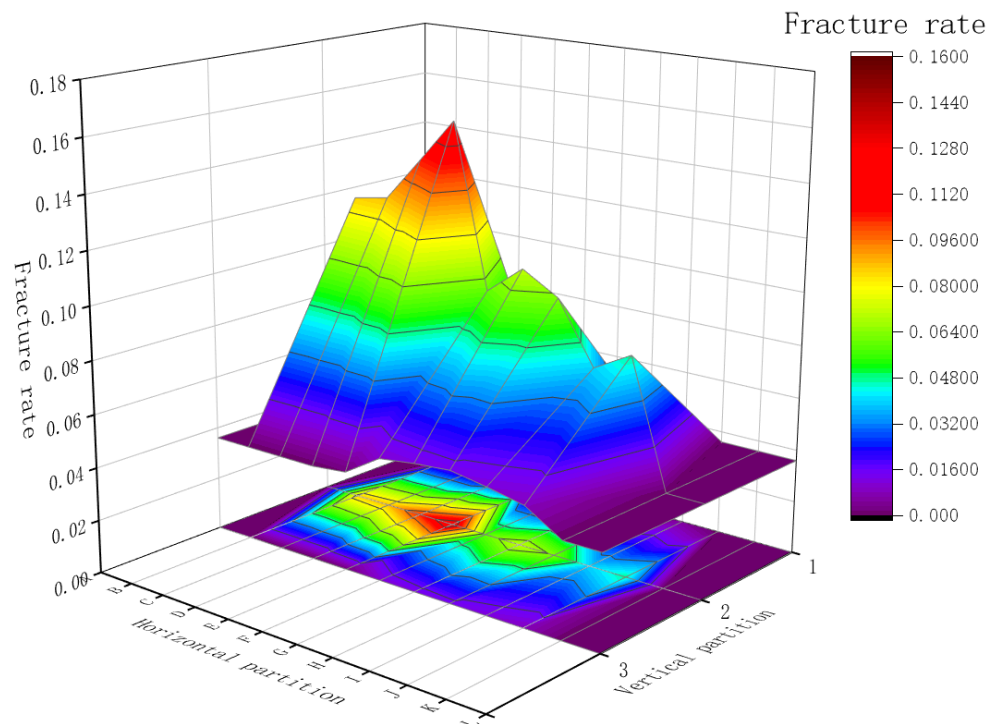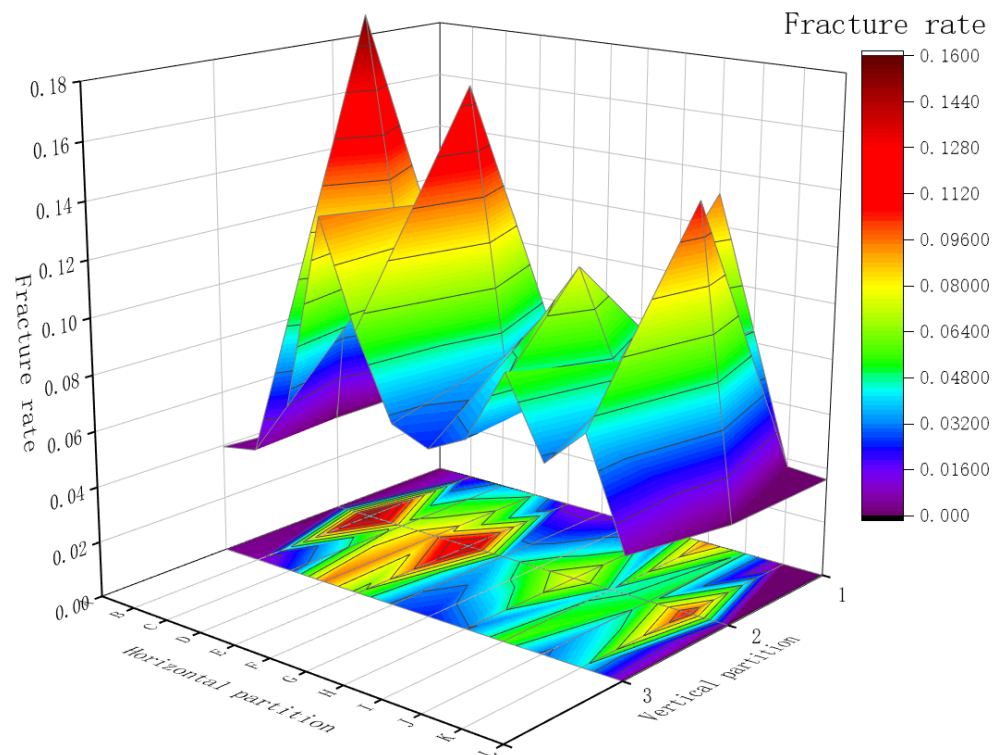

(**a**) #3 single RMA
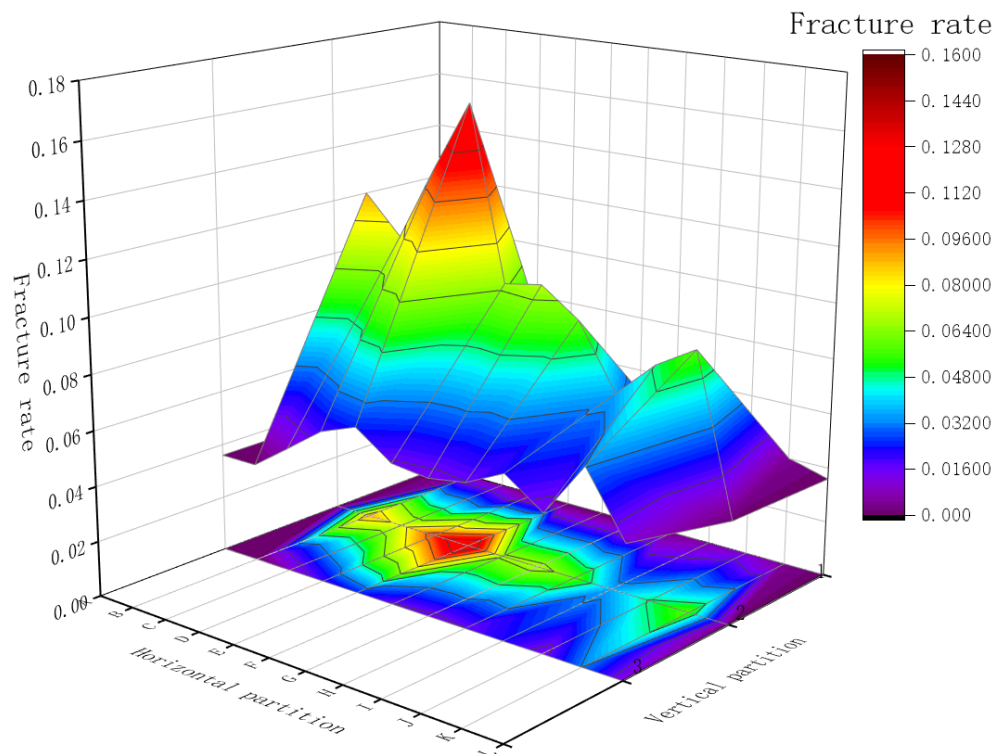
(**b**) #3 and #12 two-layer composite RMA

Figure 8. *Cont.*
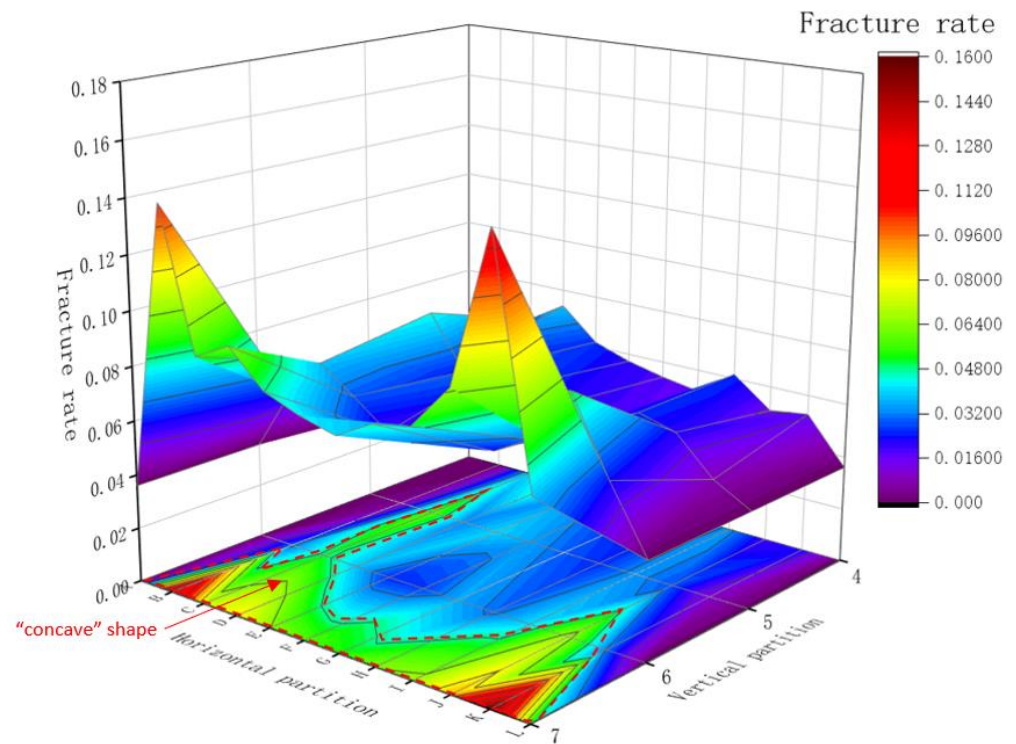
(**c**) #3, #12, and #15 three-layer composite RMA

Figure 8. A 3D surface and 2D projection diagram of the #3 RMA fracture rate.

As shown in Figure 8, the overall average fracture rate of the #3 RMA was 2.05% when the coal seam was mined out. Due to the violent pressure, which first appeared on the roof of the #3 RMA, the peak fracture rate (12.09%) occurs in the E2 grid. The overall average fracture rate increases to 2.63% after the double-layer composite RMA was formed. Two peak values of 10.27% and 12.83% were generated in the D2 and E2 grids, respectively. Moreover, the overall average fracture rate rises sharply to 4.32% when the three-layer composite RMA was formed. In this case, three peak fracture rates were generated in the B2, E2, and K2 grids, and their fracture rates are 15.48%, 13.47%, and 10.81%, respectively.

Comparing Figure 8a–c, it is clear that the increase in the overall average fracture rate was 28.29% when the #3 RMA evolved from a single to a two-layer RMA, and the increase in the overall average fracture rate rose to 64.26% when the two-layer RMA evolved to a three-layer composite RMA. Due to the reduced thickness and greater distance of the #12 and #3 RMAs, the fracture rate change induced by the caving of #12 is not obvious. Although the vertical distance between the #3 and #15 RMAs is about 1.5 times that of the vertical distance between #3 and #12 RMAs, the formation of the #15 RMA had a greater impact on the growth in the fracture rate of #3 than that induced by the caving in #12. This is because the mining thickness of the #15 coal seam was about four times that of the #12. Thus, compared with the vertical distance between the coal seams, the thickness of the excavated coal seam is the main factor affecting the growth of fracture rate for composite RMAs.

The fracture evolution law of the #12 RMA is shown in Figure 9.

As shown in Figure 9a, the overall average fracture rate of the #12 RMA was 2.89% when the #3 and #12 coal seams were mined out and formed a two-layer composite RMA. There are two peaks appearing in grids B7 and K7 on either boundary side of #12, and their fracture rates reached 10.48% and 11.92%, respectively.

(**a**) #3 and #12 two-layer composite RMA
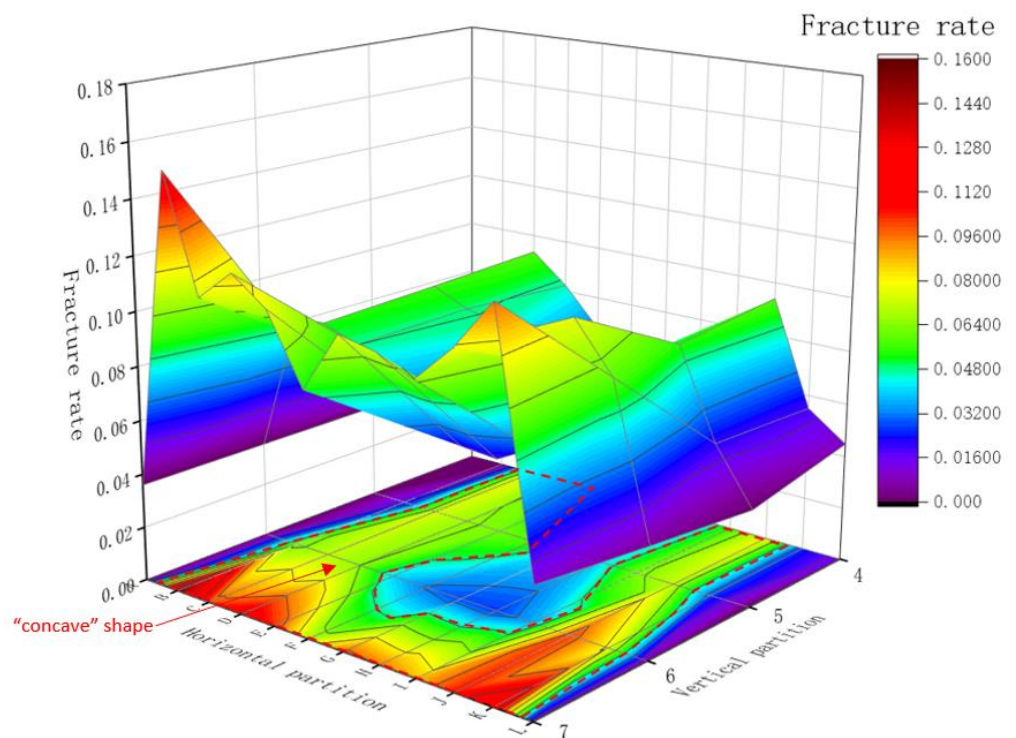
(**b**) #3, #12, and #15 three-layer composite RMA

Figure 9. A 3D surface and 2D projection diagram of the #12 RMA fracture rate.

When the #15 coal seam was mined out, the #3, #12, and #15 RMAs jointly formed a three-layer composite RMA (Figure 9b). The long-distance composite RMA is composed of #3 and #12, and the close-distance composite RMA is composed of #12 and #15 RMA. The overall average fracture rate of the #12 RMAs overlying strata increased to 4.02%. The

fracture rate of all regions between the two peaks of the #12 RMA from B7 to K7 (the red part greater than 7.20%) increased significantly. A fracture rate of greater than 4.8% shows an obvious "concave" shape area in the projection diagram (red dotted frame area). This area may be the main gas storage space and migration channel of gas in #12. Comparing the two figures of Figure 9a,b, the overall average fracture rate of the #12 RMA's overlying strata increased by 39.10%, indicating that the formation of the #15 RMA had a greater impact on the #12 RMA fracture development.

In the case of a composite RMA changing from two layers to three layers, analyzing from the vertical direction first, the #12 RMA has 4, 5, 6, and 7 partitions, and the fracture rate distribution was obtained by digital quantitative analysis. Figure 10a,b shows that the fracture rate of the three-layer composite RMA is generally greater than that of the double-layer composite RMA. Whether it is a double-layer composite RMA or a composite three-layer RMA, the average fracture rate of the four vertical partitions increases sequentially from top to bottom. The closer to the #12 RMA, the more intense the fracture growth, which shows a similar exponential growth trend. The fracture rate distribution of the A–L horizontal partitions appears as the parabolic trend in each vertical partition. In other words, the fracture rate shows high values on the boundary of two sides and low values in the middle area, producing a concave shape.

The following principles [53] are to be observed for quantitative analysis of longitudinal fracture:

(1) The fractures across the partition are counted using the principle of cutting the fractures at the partition line when counting the number of fractures in each partition of the whole composite RMA (when the same fracture spans two zones, the number of fractures is counted in each zone without affecting each other).

(2) The longitudinal and horizontal fractures in the same partition are counted according to the principle of cutting the intersection of the two. Fractures with continuous characteristics are regarded as single fractures.

(3) If the inclination angle is greater than 45°, it is regarded as a longitudinal fracture.

Due to the longitudinal fractures in the rock layer playing a leading role in gas migration between the upper and lower composite RMAs, it is necessary to study the percentage of longitudinal fractures in the total number of fractures.
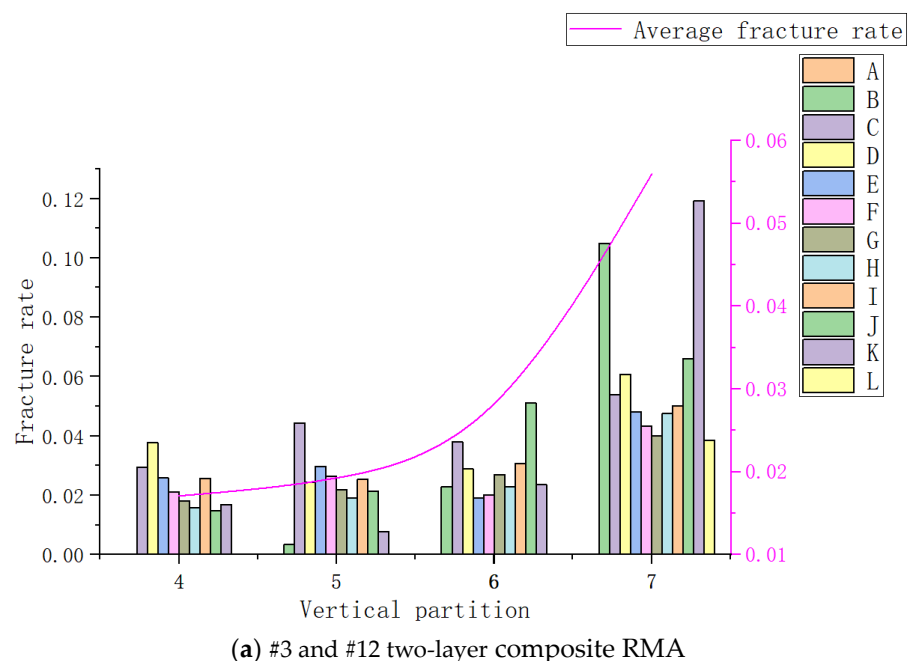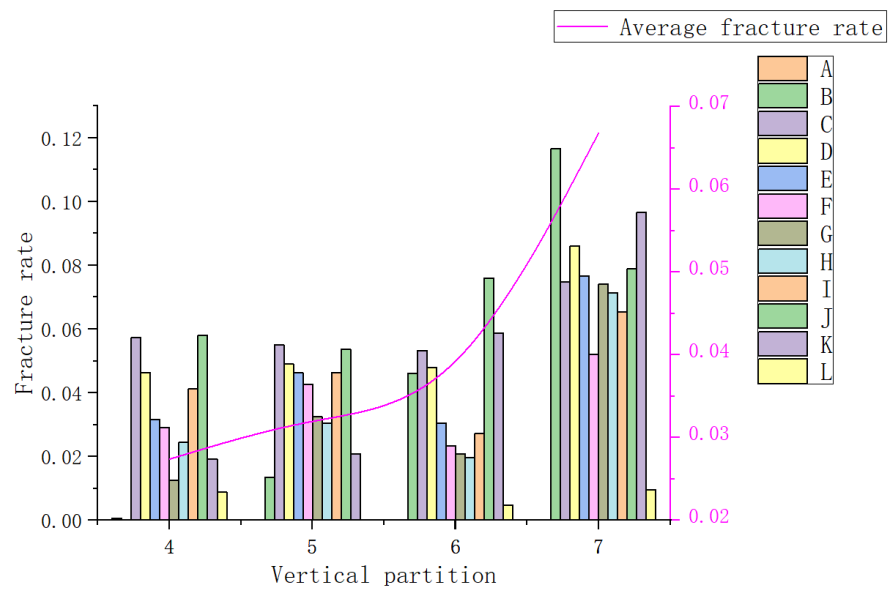

(**a**) #3 and #12 two-layer composite RMA

Figure 10. *Cont.*

(b) #3, #12, and #15 three-layer composite RMA

Figure 10. Growth trend of fracture rate in the #12 RMA.

Based on the above principles, as shown in Figure 11, curves 1–9 represent the changing trend of the strip curve of the proportion of longitudinal fractures in the three-layer RMA.
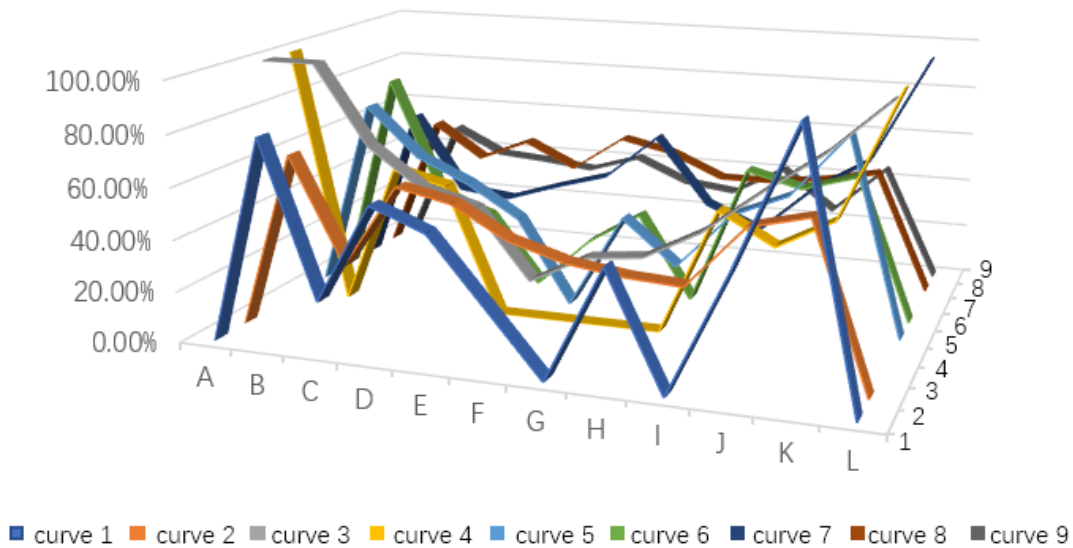

Figure 11. Line chart of longitudinal fracture proportions.

In general, the area where the proportion of longitudinal fractures is more than 60% is mainly concentrated in the A, B, C, and D partitions on the side near the open-off cut position, and in the J, K, and L partitions on the other side. The proportion of longitudinal fractures in the E, F, G, H, and I partitions in the middle area is less than 60%. The partition with a high proportion of longitudinal fractures is in the cross-layer fracture area of the composite RMA. This is the main reason for the gas flow of CBM between the strata in the cross-layer fracture area.

4.2.2. Division of Three-Layer Composite Fracture Field Area

The fracture field of the three-layer composite RMA was digitally analyzed and the distribution characteristics of the different fracture rates in different regions were obtained. The fracture field of the three-layer composite RMA was further divided into regions, as shown in Figure 12.
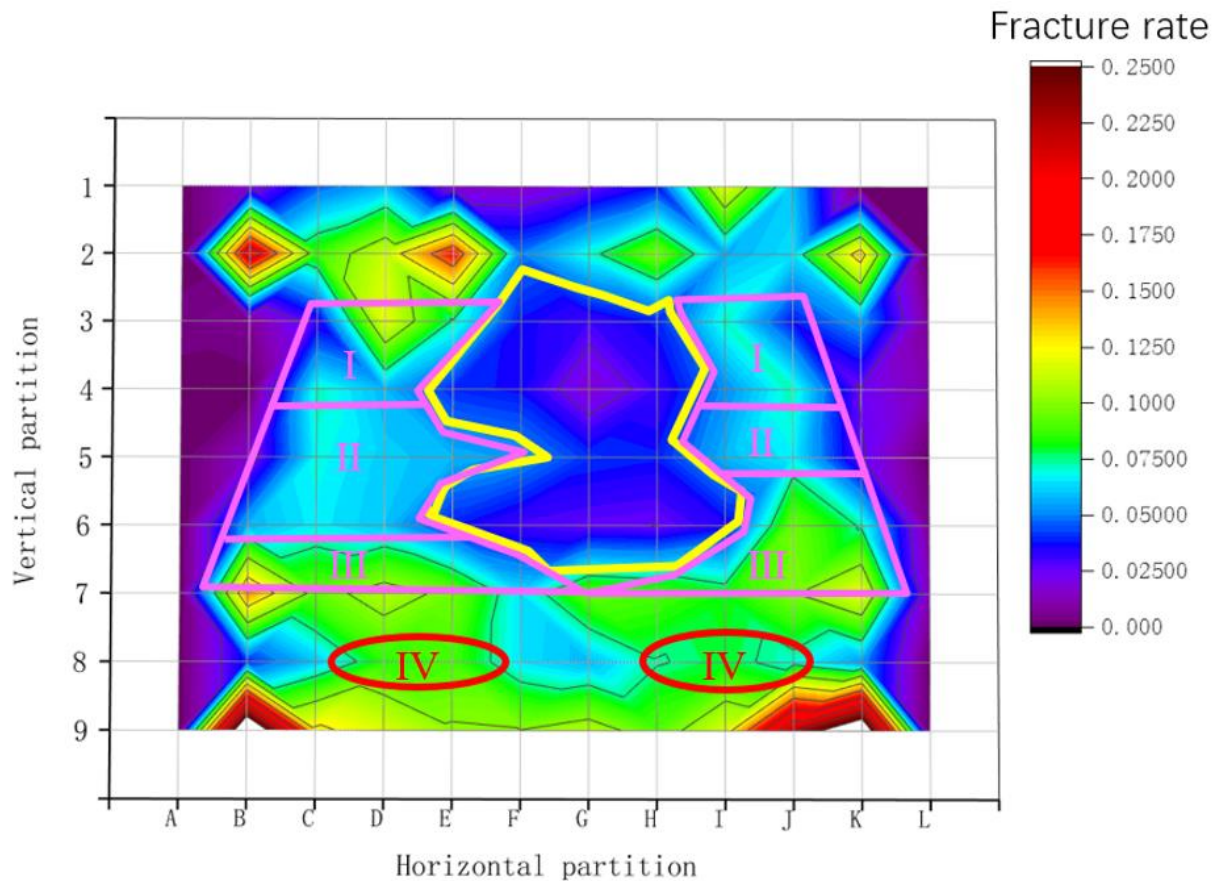
Figure 12. Fracture rate partition projection of the three-layer composite RMA. Notes: In the long-distance composite RMA: I: the cross-layer fracture connected area., II: the cross-layer fracture stability area, III: the concentrated growth area of the cross-layer fracture; IV: the connected area of cross-layer fracture in the close-distance composite RMA.

Taking the long-distance composite RMA composed of the #3 and #12 RMAs as the research object, we divided it into yellow and pink regions:

The yellow frame line area: the distribution of the central compaction area with a fracture rate ranging from 0% to 3.5% presents a gourd shape due to the existence of inferior key strata in the A5–L5 partition. When the inferior key strata are broken, there are more uncoordinated fractures on both sides of the fractured rock strata than in the surrounding rock strata. The uncoordinated fractures on both sides of the compaction area led to the partial shrinkage of the two sides of the compaction area.

The pink frame line area: the concentrated distribution area of cross-layer fractures between the #3–12 composite RMAs is located on both sides of the compaction area. According to the distribution characteristics of fracture rate and its location characteristics, it is further divided into top, middle, and bottom layers:

As shown in Area I in Figure 12, the pink frame line area at the top of the cross-layer fracture area on both sides is called the cross-layer fracture connected area and is located at the junction of the fracture connectivity of the #3 and #12 RMAs. The left fracture rate ranges from 2.5% to 9.6%, and the right fracture rate ranges from 2.9% to 5.8%.

As shown in Area II in Figure 12, the pink frame line area in the middle of the cross-layer fracture area on both sides is called the cross-layer fracture stability area and the fracture rate change is relatively stable, mainly concentrated between 4.5% and 5.5%, although the left area is still larger than the right area.

As shown in Area III in Figure 12, the pink frame line area at the bottom of the cross-layer fracture area on both sides is called the concentrated growth area of the cross-layer fracture. The fracture rate on both sides ranges from 5.8% to 12.0%, and it is the area with the most fully developed fractures and the highest fracture rate in the whole cross-layer fracture area.

Taking the close-distance composite RMA composed of #12 and #15 RMAs as the research subject:

The fracture rate of the cross-layer fracture area on both sides increases sharply in the close-distance composite RMA. It is divided and defined as the top cross-layer fracture connected area and the bottom cross-layer fracture concentrated growth area. The red oval frame line area IV in Figure 12 is the connected area of cross-layer fracture in the close-distance composite RMA. The fracture rate ranges from 5.5% to 7.5%, the left fracture range is slightly greater than that of the right side. The fracture rate in the B9–K9 area below is 7.2–24.5%, the average fracture rate in this area reaches a highest value of 12.65%, meaning it is divided into a concentrated growth area of cross-layer fractures. The range of the central compaction area is relatively small, and the fracture rate remains between 4.5% and 5.2%.

The similarities of the long-distance and close-distance composite RMAs: The cross-layer fracture area closer to the open-cut side was more disturbed during the mining process so fracture development is more frequent and wider. Therefore, for the gas extraction project site, the cross-layer fracture connected area on the side of the open-cut is a favorable extraction location for surface drilling in the composite RMA. Such a drilling arrangement can achieve "one well multi-purpose", that is, simultaneous collaborative extraction from the two-layer composite RMA. This method can effectively carry out sustainable exploitation of CBM and prevent gas disasters at the same time. Because the fracture rate of the cross-layer fracture connected area in the close-distance composite RMA is greater than that in the long-distance composite RMA, its extraction effect will be more obvious and more efficient.

5. Conclusions

In this paper, the advanced XTDIC monitoring system and a more accurate digital quantitative analysis method of fractures are used to study the fracture development characteristics of a three-layer composite RMA gas storage space. The problem that the statistical accuracy of fractures is affected by many speckles left on the rock surface when the DIC speckle technique is used in a similar simulation experiment is solved. This study will lay a solid foundation for the green and sustainable exploitation of CBM in the RMA. The main conclusions are as follows:

(1) During the evolution from single to three-layer composite RMA, the displacement region of rock layers larger than 3.5 mm has changed from an isosceles trapezoid with a narrow top and a wide bottom to a two-layer stacked trapezoid. Finally, it evolved into a huge, inverted trapezoid with a wide top and a narrow bottom and shows an upward extension trend. As the number of RMAs below increases, the angle and range of the displacement area of rock strata in the whole composite RMA increase radially.

(2) The fracture rate of the same area in a composite RMA is greater than that of a single one. When the single RMA evolves into a two-layer and three-layer composite RMA, the uppermost RMA overall average fracture rate increases by 28.29% and 64.26%, respectively. Compared with the vertical distance between the RMAs, mining thickness is the main factor affecting the growth of fractures in a composite RMA.

(3) In the long-distance composite RMA, the overburden fracture rate shows an approximately exponential growth trend from top to bottom. The fracture rate shows a parabolic trend distribution in the horizontal partition, showing a concave shape with highs on both sides and a low in the middle. The overall fracture rate of the close-distance composite RMA increases more sharply, the average fracture rate in the concentrated growth area is 12.65%, which reached the highest value in the three-layer RMA. The number of longitudinal fractures on both sides of the composite RMA accounts for more than 60% of total fractures, which indicates that the cross-layer fracture area is the main migration channel for CBM.

(4) The mining disturbance of the cross-layer fracture area near the open-cut is greater than that on the other side, so the occupied area and its average fracture rate are greater than those on the stopping side. In engineering applications, the cross-layer fracture connected area on the side of the open-cut is a favorable extraction location for surface drilling in the composite RMA, which can effectively control and extract the CBM in the composite RMA.

Institutional Review Board Statement: Not applicable.

Informed Consent Statement: Not applicable.

Data Availability Statement: Data available on request due to privacy restrictions.

Conflicts of Interest: The authors declare no conflict of interest.

References

1. McGlade, C.; Speirs, J.; Sorrell, S. Unconventional gas—A review of regional and global resource estimates. *J. Energy* **2013**, *55*, 571–584. [CrossRef]
2. Zhang, Y.J.; Feng, G.R.; Zhang, M.; Ren, H.R.; Bai, J.W.; Guo, Y.X.; Jiang, H.N.; Kang, L.X. Residual coal exploitation and its impact on sustainable development of the coal industry in China. *J. Energy Policy* **2016**, *96*, 534–541. [CrossRef]
3. Feng, G.R.; Zhang, Y.J.; Qi, T.Y.; Kang, L.X. Status and research progress for residual coal mining in China. *J. China Coal Soc.* **2020**, *45*, 151–159.
4. Karacan, C.O.; Ruiz, F.A.; Cote, M.; Phipps, S. Coal mine methane: A review of capture and utilization practices with benefits to mining safety and to greenhouse gas reduction. *Int. J. Coal Geol.* **2011**, *86*, 121–156. [CrossRef]
5. Black, D.J.; Aziz, N.I. Developments in coal mine methane drainage and utilisation in Australia. In Proceedings of the Ninth International Mine Ventilation Congress, New Delhi, India, 10–13 November 2009.
6. Feng, G.R.; Zhao, J.P.; Wang, H.W.; Li, Z.; Fang, Z.L.; Fan, W.C.; Yang, P.; Yang, X.J. Study of the internal re-breaking characteristics of broken limestone during compression. *J. Powder Technol.* **2022**, *396*, 449–455. [CrossRef]
7. Kirchgessner, D.A.; Piccot, S.D.; Masemore, S.S. An improved inventory of methane emissions from coal mining in the United States. *J. Air Waste Manag. Assoc.* **2000**, *50*, 1904–1919. [CrossRef] [PubMed]
8. Warmuzinski, K. Harnessing methane emissions from coal mining. *Process Saf. Environ. Prot.* **2008**, *86*, 315–320. [CrossRef]
9. Pach, G.; Zenon, R.; Wrona, P. Developments in coal mine methane drainage and utilisation of The Upper Silesia. 2014.
10. Karacan, C.O.; Warwick, P.D. Assessment of coal mine methane (CMM) and abandoned mine methane (AMM) resource potential of longwall mine panels: Example from Northern Appalachian Basin, USA. *Int. J. Coal Geol.* **2019**, *208*, 37–53. [CrossRef]
11. Shimada, H.; Chen, Y.L.; Hamanaka, A.; Sasaoka, T.; Shimada, H.; Matsui, K. Application of Highwall Mining System to Recover Residual Coal in End-walls. In Proceedings of the Procedia Earth and Planetary Science, International Symposium on Earth Science and Technology, Bandung, Indonesia, 18–19 September 2012.
12. Mazzotti, M.; Pini, R.; Storti, G. Enhanced coalbed methane recovery. *J. Supercrit. Fluids* **2009**, *47*, 619–627. [CrossRef]

13. Creedy, D.P.; Garne, R.K.; Holloway, S.; Ren, T.X. *A Review of the Worldwide Status of Coalbed Methane Extraction and Utilisation*; Wardell Armstrong, British Geological Survey, University of Nottingham: Nottingham, UK, 2001; pp. 28–34.
14. Tao, S.; Pan, Z.J.; Tang, S.L.; Chen, S.D. Current status and geological conditions for the applicability of CBM drilling technologies in China: A review. *Int. J. Coal Geol.* **2019**, *202*, 95–108. [CrossRef]
15. Karmis, M.; Triplett, T.; Haycocks, C.; Goodman, G. Mining subsidence and its prediction in Appalachian coalfield. In Proceedings of the Proceedings—Symposium on Rock Mechanics, College Station, Texas, 20–23 June 1983; pp. 665–675.
16. Peng, S.S. *Longwall Mining*; Society for Mining Metallurgy and Exploration: Englewood, CO, USA, 1984.
17. Li, Z.; Feng, G.R.; Jiang, H.N.; Hu, S.Y.; Cui, J.Q.; Song, C.; Gao, Q.; Qi, T.Y.; Guo, X.Q.; Li, C.; et al. The correlation between crushed coal porosity and permeability under various methane pressure gradients: A case study using Jincheng anthracite. *Greenh. Gases Sci. Technol.* **2018**, *8*, 493–509. [CrossRef]
18. Lin, T.Q. Influence of Mining activities on mine rock mass and control engineering. *J. China Coal Soc.* **1995**, *20*, 1–5.
19. Qian, M.G.; Xu, J.L. Study on the "O-SHAPE" circle distribution characteristics of mining-induced fractures in the overlaying strata. *J. China Coal Soc.* **1998**, *23*, 466–469.
20. Li, S.G.; Lin, H.F.; Zhao, P.X.; Xiao, P.; Pan, H.Y. Dynamic evolution of mining fissure elliptic paraboloid zone and extraction coal and gas. *J. China Coal Soc.* **2014**, *39*, 1455–1462.
21. Qin, W.; Xu, J.L. Horizontal Subzone Characteristics and Methane Seepage Properties of the Gas Flowing Fracture Zone above the Gob. *Adv. Civ. Eng.* **2018**, *2018*, 9071578. [CrossRef]
22. Xie, G.X.; Yang, K. Study of macro stress shell evolving characteristics of rock surrounding face. *Chin. J. Rock Mech. Eng.* **2010**, *29*, 2676–2680.
23. Xu, J.L.; Qian, M.G.; Jin, H.W. Study on "coal and coal-bed methane simultaneous extraction" technique on the basis of strata movement. *J. China Coal Soc.* **2004**, *29*, 129–132.
24. Karacan, C.; Goodman, G. Hydraulic conductivity changes and influencing factors in longwall overburden determined by slug tests in gob gas ventholes. *Int. J. Rock Mech. Min. Sci.* **2009**, *46*, 1162–1174. [CrossRef]
25. Liu, X.Y. Experimental Study of Dynamic Development and Fractal law of Mining Rock Fracture. *Appl. Mech. Mater.* **2011**, *71–78*, 3428–3432. [CrossRef]
26. Xu, P.; Li, S.; Lin, H.; Ding, Y.; Shuang, H.; Liu, S.; Tian, Y. Fractal Characterization of Pressure-Relief Gas Permeability Evolution in a Mining Fracture Network. *Energies* **2021**, *14*, 7031. [CrossRef]
27. Majdi, A.; Hassani, F.; Nasiri, M. Prediction of the height of destressed zone above the mined panel roof in longwall coal mining. *Int. J. Coal Geol.* **2012**, *98*, 62–72. [CrossRef]
28. Poulsen, B.A.; Adhikary, D.; Guo, H. Simulating mining-induced strata permeability changes. *Eng. Geol.* **2018**, *237*, 208–216. [CrossRef]
29. Li, Z. *Research on the Deformation and Seepage Characteristics of Crushed Coal and Rock and Its Application in Abandoned Coal Mine Gob Methane Extraction*; D. Taiyuan University of Technology: Taiyuan, China, 2018.
30. Xu, Y.Y. *Coal Mining*; M. China University of Mining and Technology Press: Xuzhou, China, 1999.
31. Liu, H.Y.; Cheng, Y.P.; Zhou, H.X.; Wang, H.F.; Yu, Q.X. Study on the Influence of Mining-induced Fracture Development of Super-long Distance Protected Layer on Pressure Relief Gas Extraction. In Proceedings of the 2007 China (Huainan) International Conference on Coal Mine Gas Control Technology, China; 2007; pp. 140–147.
32. Li, S.Q.; He, X.Q.; Li, S.Q.; Zhang, S.J.; Yan, Z.; Xie, Q.X.; Ding, Y. Experimental research on strata movement and fracture dynamic evolution of double pressure-relief mining in coal seams group. *J. China Coal Soc.* **2013**, *38*, 2146–2152.
33. Ma, H.F.; Cheng, Z.H.; Liu, W. Evolution characteristics of mining stress and overlying strata displacement field under superimposed mining in close distance coal seam group. *J. Saf. Sci. Technol.* **2017**, *13*, 28–33.
34. Karacan, C.O.; Esterhuizen, G.S.; Schatzel, S.J.; Diamond, W.P. Reservoir simulation-based modeling for characterizing longwall methane emissions and gob gas venthole production. *Int. J. Coal Geol.* **2007**, *71*, 225–245. [CrossRef]
35. Hu, Y.Z.; Liu, C.Q.; Liu, C.Y.; Xhen, B.B. Development regularity of mining-induced fractures in mixed mining of coal seam group. *J. Min. Saf. Eng.* **2015**, *32*, 396–400.
36. Si, G.; Jamnikar, S.; Lazar, J.; Shi, J.Q.; Durucan, S.; Korre, A.; Zavsek, S. Monitoring and modelling of gas dynamics in multi-level longwall top coal caving of ultra-thick coal seams, part I: Borehole measurements and a conceptual model for gas emission zones. *Int. J. Coal Geol.* **2015**, *144*, 98–110. [CrossRef]
37. Qin, W.; Xu, J.L.; Peng, X.Y.; Hu, G.Z. Optimal layout of surface borehole network for gas drainage from abandoned gob. *J. Min. Saf. Eng.* **2013**, *30*, 289–295.
38. Qin, W.; Xu, J.L.; Hu, G.Z. Optimization of abandoned gob methane drainage through well placement selection. *J. Nat. Gas Sci. Eng.* **2015**, *25*, 148–158. [CrossRef]
39. Zhuo, H.; Qin, B.T.; Shi, Q.L.; Li, L. Development law of air leakage fractures in shallow coal seams: A case study in the Shendong Coalfield of China. *Environ. Earth Sci.* **2018**, *77*, 772. [CrossRef]
40. Huang, Q.X.; Du, J.W.; Hou, E.K.; Yang, F. Research on overburden and ground surface cracks distribution and formation mechanism in shallow coal seams group mining. *J. Min. Saf. Eng.* **2019**, *36*, 7.
41. Tian, C.L.; Liu, Y.B.; Yang, X.L.; Hu, Q.T.; Wang, B.; Yang, H.M. Development characteristics and field detection of overburden fracture zone in multiseam mining: A case study. *Energy Sci. Eng.* **2020**, *8*, 602–615. [CrossRef]
42. Liu, Y.B.; Cheng, J.L.; Jiao, J.J.; Meng, X.X. Feasibility study on multi-seam upward mining of multi-layer soft-hard alternate complex roof. *Environ. Earth Sci.* **2022**, *81*, 424. [CrossRef]

43. Wu, Q.Y.; Guo, Z.W.; Zhai, H.L.; Wang, J.W.; Zhang, M.J.; Chi, B.S.; Wang, E.Y.; Guo, S.Q. Physical simulation on spatial distribution of void fraction in overburden due to repeated mining in North Shaanxi Mining Area. *Coal Sci. Technol.* **2022**, *50*, 105–111.

44. Riley, P.; Crowe, P. Airborne and Terrestrial Laser Scanning-Applications for Illawarra Coal. In *Coal Operators' Conference*; Aziz, N., Ed.; University of Wollongong & the Australasian Institute of Mining and Metallurgy: Wollongong, NSW, Australia, 2006; pp. 266–275.

45. Berkovic, G.; Shafir, E. Optical methods for distance and displacement measurements. *Adv. Opt. Photon.* **2012**, *4*, 441–471. [CrossRef]

46. Kashfuddoja, M.; Prasath, R.G.R.; Ramji, M. Study on experimental characterization of carbon fiber reinforced polymer panel using digital image correlation: A sensitivity analysis. *Opt. Lasers Eng.* **2014**, *62*, 17–30. [CrossRef]

47. Zhou, Y.; Sun, C.; Song, Y.; Chen, J. Image pre-filtering for measurement error reduction in digital image correlation. *Opt. Lasers Eng.* **2015**, *65*, 46–56. [CrossRef]

48. Palamara, D.R.; Nicholson, M.; Flentje, P.; Baafi, E.; Brassington, G.M. An evaluation of airborne laser scan data for coalmine subsidence mapping. *Int. J. Remote Sens.* **2007**, *28*, 3181–3203. [CrossRef]

49. Feng, F.; Chen, S.J.; Wang, Y.J.; Huang, W.P.; Han, Z.Y. Cracking mechanism and strength criteria evaluation of granite affected by intermediate principal stresses subjected to unloading stress state. *Int. J. Rock Mech. Min. Sci.* **2021**, *143*, 10473. [CrossRef]

50. Chen, S.J.; Feng, F.; Wang, Y.J.; Li, D.Y.; Huang, W.P.; Zhao, X.D.; Jiang, N. Tunnel failure in hard rock with multiple weak planes due to excavation unloading of in-situ stress. *J. Cent. South Univ.* **2020**, *27*, 2864–2882. [CrossRef]

51. Feng, F.; Xie, Z.W.; Xue, T.X.; Wang, E.Y.; Huang, R.F.; Li, X.L.; Gao, S.X. Application of a combined FEM/DEM approach for teaching a deep rock mass mechanics course. *Sustainability* **2023**, *15*, 937. [CrossRef]

52. Smith, J.; Ghabraie, B.; Ren, G.; Holden, L. Application of 3D laser scanner, optical transducers and digital image processing techniques in physical modelling of mining-related strata movement. *Int. J. Rock Mech. Min. Sci.* **2015**, *100*, 219–230.

53. Hu, L.Q. *The Evolution Law of the Dominant Channel of Pressure Relief Gas in the Overburden Cracks in the Mining Area*; D. Taiyuan University of Technology: Taiyuan, China, 2021.

54. Feng, G.R.; Li, Z.; Hu, S.Y.; Zhng, Y.T.; Zhang, A.; Gao, Q.; Jiang, H.N.; Guo, X.Q.; Li, C.; Cui, J.Q. Distribution of gob empty space for methane drainage during the longwall mining: A case study. *J. Nat. Gas Sci. Eng.* **2018**, *60*, 112–124. [CrossRef]

55. Zhang, C.W. *Formation Mechanism and Multi-Scale Seepage Characteristics of Overburden Fracture in Abandoned Coal Mine*; D. Taiyuan University of Technology: Taiyuan, China, 2021.

56. Wang, H.W.; Zhou, H.W.; Zuo, J.P. Application of optical measurement method in strata movement simulation experiment. *J. China Coal Soc.* **2006**, *31*, 278–281.

57. Chew, K.S.; Zarrabi, K. Non-contact displacements measurement using an improved particle swarm optimization based digital speckle correlation method. In Proceedings of the International Conference on Pattern Analysis and Intelligent Robotics ICPAIR 2011, Kuala Lumpur, Malaysia, 28–29 June 2011.

58. Xiao, X.C.; Pan, Y.S.; Lv, X.F. Experimental study of deep depth tunnel surrounding rock burst proneness with equivalent material simulating method based on digital speckle correlation technique. *J. China Coal Soc.* **2011**, *36*, 1629–1635.

59. Yuan, C.F.; Yuan, Z.J.; Wang, Y.T.; Li, C.M. Analysis of the diffusion process of mining overburden separation strata based on the digital speckle correlation coefficient field. *Int. J. Rock Mech. Min. Sci.* **2019**, *119*, 13–21. [CrossRef]

60. Zhang, L.F.; Chen, Z.H.; Nian, G.Q.; Bao, M.; Zhou, Z.H. Base friction testing methodology for the deformation of rock masses caused by mining in an open-pit slope. *Measurement* **2023**, *206*, 112–235. [CrossRef]

61. Ren, W.Z.; Guo, C.M.; Peng, Z.Q.; Wang, Y.G. Model experimental research on deformation and subsidence characteristics of ground and wall rock due to mining under thick overlying terrane. *Int. J. Rock Mech. Min. Sci.* **2010**, *47*, 614–624. [CrossRef]